

## Diagnosis of Subtropical Humidity Dynamics Using Tracers of Last Saturation

JOSEPH GALEWSKY AND ADAM SOBEL

*Department of Applied Physics and Applied Mathematics, Columbia University, New York, New York*

ISAAC HELD

*NOAA/Geophysical Fluid Dynamics Laboratory, Princeton University, Princeton, New Jersey*

(Manuscript received 5 April 2004, in final form 8 January 2005)

### ABSTRACT

A technique for diagnosing the mechanisms that control the humidity in a general circulation model (GCM) or observationally derived meteorological analysis dataset is presented. The technique involves defining a large number of tracers, each of which represents air that has last been saturated in a particular region of the atmosphere. The time-mean tracer fields show the typical pathways that air parcels take between one occurrence of saturation and the next. The tracers provide useful information about how different regions of the atmosphere influence the humidity elsewhere. Because saturation vapor pressure is a function only of temperature and assuming mixing ratio is conserved for unsaturated parcels, these tracer fields can also be used together with the temperature field to reconstruct the water vapor field. The technique is first applied to an idealized GCM in which the dynamics are dry and forced using the Held–Suarez thermal relaxation, but the model carries a passive waterlike tracer that is emitted at the surface and lost due to large-scale condensation with zero latent heat release and no condensate retained. The technique provides an accurate reconstruction of the simulated water vapor field. In this model, the dry air in the subtropical troposphere is produced primarily by isentropic transport and is moistened somewhat by mixing with air from lower levels, which has not been saturated since last contact with the surface. The technique is then applied to the NCEP–NCAR reanalysis data from December–February (DJF) 2001/02, using the offline tracer transport model MATCH. The results show that the dryness of the subtropical troposphere is primarily controlled by isentropic transport of very dry air by midlatitude eddies and that diabatic descent from the tropical upper troposphere plays a secondary role in controlling the dryness of the subtropics.

### 1. Introduction

The dry regions of the subtropical free troposphere play an important role in the radiative balance of the earth's climate (Held and Soden 2000; Pierrehumbert 1995). The dryness of these regions has generally been attributed to the radiative cooling and cross-isentropic subsidence of dehydrated air detraining from deep convective towers at the top of the Hadley circulation (Spencer and Braswell 1997; Sun and Lindzen 1993) with additional moistening from lateral advection of moist air from the convective regions (Pierrehumbert and Roca 1998; Soden 1998; Salathe and Hartmann

1997; Sherwood 1996) or from the evaporation of hydrometeors (Sun and Lindzen 1993). Isentropic transport by extratropical eddies has also been identified as a mechanism for dehydrating extratropical air (Kelly et al. 1991; Yang and Pierrehumbert 1994), but its relative importance for drying the subtropics has not been quantified.

Our understanding of these mechanisms has been simplified by the recent finding that the observed humidity distribution in the troposphere can, to first order, be reconstructed by considering the large-scale circulation as given and using it to advect a passive waterlike tracer, without any explicit parameterization of convection or cloud microphysics (Sherwood 1996; Salathe and Hartmann 1997; Pierrehumbert and Roca 1998; Dessler and Sherwood 2000). The tracer is assumed to condense, and all condensate immediately removed when the temperature reaches the dewpoint.

---

*Corresponding author address:* Dr. Joseph Galewsky, Department of Earth and Planetary Sciences, University of New Mexico, Albuquerque, NM 87131.  
E-mail: galewsky@unm.edu

Latent heat release is not explicitly considered, though information about convective heating is implicit in the circulation being used for the advection.

In this simplified picture, one can assume that upward motion leads to saturation and the consequent removal of all condensate, leaving parcels exactly saturated when their ascent ceases. Once these parcels begin descending and warming in downward branches of the circulation, they conserve water vapor mixing ratio until they either ascend and saturate again or come in contact with the surface where water vapor is emitted. Up to that point, one can think of the mixing ratio of each parcel as having been set by the saturation vapor pressure at the temperature at which it was last saturated. Because of mixing, an air parcel's water vapor mixing ratio represents an average over a spectrum of last saturation temperatures determined by the paths of the different subparcels that constitute the parcel.

Here we present a technique for diagnosing the mechanisms that control the humidity in general circulation models (GCMs) and in reanalysis data. The technique is based on the concepts of large-scale advection and last saturation described above, and is closely related to Green's function or boundary propagator methods (Hall and Plumb 1994; Holzer and Hall 2000; Haine and Hall 2002) as well as, somewhat less directly, the transilient matrix approach (Stull 1984; Ebert et al. 1989; Stull 1993; Sobel 1999; Larson 1999), all of which have been applied in different contexts. This technique is complementary to the Lagrangian back-trajectory techniques that have been used in previous studies of tropospheric humidity (Salathe and Hartmann 1997; Pierrehumbert 1998; Soden 1998; Pierrehumbert and Roca 1998) in that it allows one to focus on the importance of specific regions of last saturation for the global humidity distribution. The technique presented here differs from these Lagrangian techniques in that it works with gridded fields rather than Lagrangian parcels (thus, discretizing the space in a more regular way) and uses the same advection algorithm as the underlying GCM.

We first apply our technique to an idealized atmospheric GCM. Dynamically, our GCM is a dry model, thermally forced by relaxation to a prescribed equilibrium state (Held and Suarez 1994). It carries a passive water vapor-like tracer, which condenses according to the Clausius-Clapeyron relation obeyed by real water vapor, but whose latent heat of vaporization is set to zero, so that it does not influence the flow. This idealized model does not contain any convective or planetary boundary layer parameterizations nor does it carry any condensate. This model is useful for testing

our diagnostic technique since any errors that occur can be ascribed to the discretization and averaging, which the technique employs, rather than to cloud microphysics or other subgrid-scale processes, which our model does not contain. We then apply the method to the National Centers for Environmental Prediction-National Center for Atmospheric Research (NCEP-NCAR) reanalysis data for the Northern Hemisphere winter 2001/02 using an offline tracer transport model that uses archived reanalysis winds and temperatures. This technique is used to quantify the relative importance of isentropic and cross-isentropic mixing in controlling the humidity of the subtropical free troposphere.

## 2. Tracer calculation

We divide a global model domain into  $N$  axisymmetric subdomains,  $\mathcal{D}_i$ , where  $i$  is an index ranging from 1 to  $N$ . Each subdomain  $\mathcal{D}_i$  is associated with a tracer,  $\mathcal{T}_i$ . Each grid cell in the model domain is thereby associated with a subdomain and a tracer. All tracers are defined over the entire global domain, but are associated with their subdomains in the following way.

Consider a saturated grid cell with latitude  $\phi$ , pressure  $p$ , and longitude  $\lambda$ . This cell resides in one of the  $N$  subdomains,  $\mathcal{D}_i$ , and is therefore associated with a tracer  $\mathcal{T}_i$ . Upon saturation in that cell, we set  $\mathcal{T}_i$  to unity,

$$\mathcal{T}_i(\phi, p, \lambda) = 1, \quad (1)$$

and we set all the remaining ( $N - 1$ ) tracers to zero at that point,

$$\mathcal{T}_j(\phi, p, \lambda) = 0, \quad (2)$$

where  $j$  takes on all values from 1 to  $N$  except  $i$ . Apart from the above operation, which is performed whenever saturation occurs in the model, and apart from a special treatment of a shallow layer near the surface (described below), all the tracers are simply advected by the large-scale flow.

If a particular tracer's value is exactly 1 in a given cell (not necessarily within the same subdomain associated with the tracer in question), it means that all of the air in that cell was last saturated in the subdomain associated with the tracer. Because of mixing, a cell generally contains a mixture of air last saturated in multiple subdomains so that any individual tracer value is usually less than 1 in unsaturated cells. The value of an individual subdomain's tracer in a particular cell can be interpreted as the probability that the air in that cell was last saturated in that tracer's subdomain. If a state were to be reached in which all of the air in a given cell

had been saturated at least once, the tracers would sum to unity,

$$\sum_{i=1}^N \mathcal{T}_i = 1, \quad (3)$$

in that cell. This is approximately true at upper levels, but not necessarily close to the surface where fresh water vapor has recently been emitted. We define a special tracer, referred to here as the source tracer, to handle this. At each time step, the source tracer is set equal to the water vapor mixing ratio at all points in a shallow surface layer. Here we define this shallow surface layer as the lowest model level, which spans the lowest 50 hPa in our idealized model described below and the lowest 30 hPa in the offline tracer transport model used for the reanalysis data. Although we have chosen to define the source tracer in terms of the lowest model level, it could also be chosen to span multiple model levels. All of the other tracers are set to zero in the shallow surface layer, whose top is located at pressure  $p_b$ :

$$\begin{aligned} S(\phi, p > p_b, \lambda) &= r(\phi, p > p_b, \lambda) \\ \mathcal{T}_i(\phi, p > p_b, \lambda) &= 0 \end{aligned} \quad (4)$$

for all  $i$ ,  $\phi$ ,  $\lambda$ , where  $S$  is the source tracer and  $r$  is the water vapor mixing ratio. When air is saturated in any cell above the shallow surface layer, the source tracer in that cell is set to zero.

The tracers can be used, together with the saturation mixing ratios determined by the temperature field in the respective subdomains, to reconstruct the water vapor field. Let us first consider a case in which the all atmospheric fields (temperature, humidity, winds, etc.) are axisymmetric and steady, so all quantities are functions of latitude and pressure only. In the limit of infinite resolution in the subdomains ( $N \rightarrow \infty$ ), or equivalently if the saturation mixing ratio were uniform in each subdomain, we would have, exactly,

$$r(\phi, p) = \iint \mathcal{T}(\phi, p|\phi', p') r^*(\phi', p') d\phi' dp' + S(\phi, p), \quad (5)$$

where now there is a tracer  $\mathcal{T}(\phi, p|\phi', p')$  for every spatial point  $(\phi', p')$  at which saturation may have occurred. In discrete form, again with  $i$  indexing the locations of last saturation, (5) becomes

$$r(\phi, p) = \sum_{i=1}^N \mathcal{T}_i(\phi, p) r_i^* + S(\phi, p), \quad (6)$$

where  $r_i^*$  denotes the saturation mixing ratio in subdomain  $i$ . Within each term in the sum (which dominates  $S$  above the near-surface levels), the two terms in the

product, the tracer and the saturation mixing ratio, encapsulate the roles of circulation and temperature, respectively. Here  $r_i^*$  is a function of the temperature and pressure in subdomain  $i$ , but under earthlike conditions we are safe in assuming that the temperature dependence dominates variations in  $r_i^*$ .

In practice, we do not have an axisymmetric and steady circulation. In the calculations below, our domains will be axisymmetric to keep  $N$  sufficiently small to make the calculations feasible. The tracers themselves will be functions of all three spatial dimensions as well as time, but in almost all of our analysis of them we will use only their zonal and time means. The last mixing ratios values  $r_i^*$  will also be zonal and time means. This introduces errors because it implies an assumption that an air parcel that experienced last saturation at some given location  $(\phi, p, \lambda, t)$  was imprinted at that time with the zonal and time mean saturation mixing ratio at  $(\phi, p)$ . In reality, there are temporal and zonal temperature variations, so the saturation mixing ratio may have been different from the zonal and time mean value. It is straightforward to show that, if these temperature variations are correlated (positively or negatively) with variations in the probability of saturation, rectified errors occur that render (6) no longer exact when phrased in terms of the zonal and time means. These errors are similar to those associated with ‘‘convective structure memory’’ in the theory of transient matrices (Ebert et al. 1989; Stull 1993; Sobel 1999; Larson 1999).

Perhaps more important than the zonal and time averaging is the fact that the subdomain size is finite. Since each tracer requires a separate advection–diffusion calculation, computational expense increases rapidly as subdomain size decreases, and in practice we must use subdomains sufficiently large that the saturation mixing ratio varies considerably within each subdomain. The most naive approach would be to use the average saturation mixing ratio over the subdomain in place of  $r_i^*$ , above. In fact, we can do somewhat better than this. We break the zonal and time mean tracer fields into two components, a ‘‘local’’ component,  $\hat{\mathcal{T}}$ , and a ‘‘nonlocal’’ component,  $\tilde{\mathcal{T}}$  (Fig. 1). The local component refers to the tracer within its own subdomain. Typically, when a given tracer has a significantly nonzero value in its own subdomain, that is because the air is either saturated at the moment or has been saturated very recently; this tends to happen in subdomains located in ascending branches of the general circulation. In this situation, we can use the fact that we know the distribution of saturation mixing ratio within the subdomain and use the local value at the grid cell in question, rather than the average over the subdomain, in the

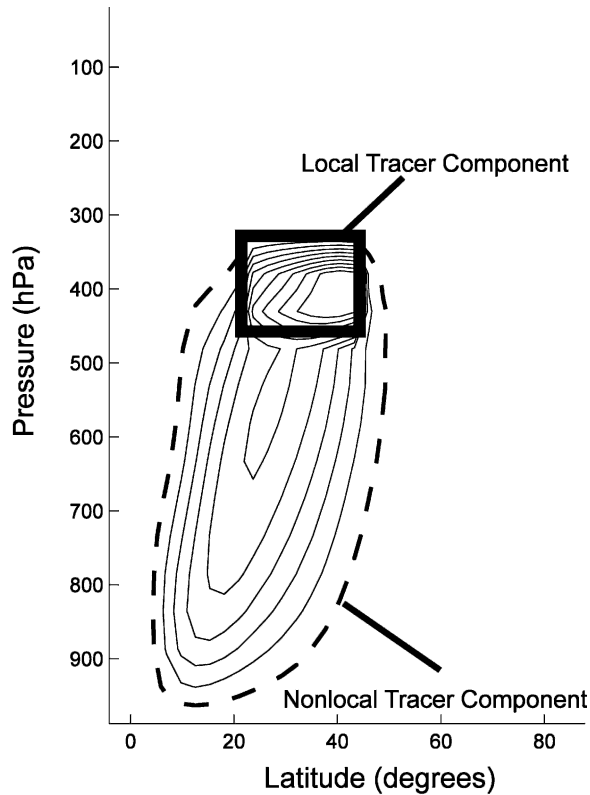


FIG. 1. Example tracer field illustrating how tracers are divided into local and nonlocal components. Contours indicate relative tracer concentration.

reconstruction of the humidity field. While it need not be true that the air is saturated precisely at that cell, the assumption that this is the case is considerably better than the assumption that it was last saturated at the average temperature of the subdomain. The nonlocal tracer component refers to the tracer everywhere outside of its own subdomain. In this case, all we know is that last saturation occurred somewhere within that tracer's subdomain; we do not know at what point within the subdomain it occurred. Therefore, for the nonlocal tracer we must use the average saturation mixing ratio from the subdomain. Thus, our finite-resolution formulation for reconstructing the zonal and time mean water vapor distribution from the tracers and the saturation mixing ratio field is

$$r_e(\phi, p) = \sum_i \hat{T}_i(\phi, p) r_i^*(\phi, p) + \sum_i \check{T}_i(\phi, p) \langle r_i^* \rangle + S, \quad (7)$$

where  $r_e$  is the reconstructed mixing ratio,  $r^*$  is the saturation mixing ratio,  $\langle r_i^* \rangle$  is the density-weighted mean of the saturation mixing ratio within the  $i$ th subdomain, and where now all fields should be read as zonal and time means. This formulation gives consid-

erably more accurate results than does simply replacing  $r_i^*$  by  $\langle r_i^* \rangle$  at all points in (6).

Because we are focusing on the troposphere, we do not actually cover the entire model atmosphere with subdomains defining associated tracers, but only define subdomains covering the region below the tropopause. The tropopause is largely, though not entirely, a transport barrier, separating air masses of different properties. If we define subdomains straddling the tropopause, particularly in the Tropics and subtropics, air descending from just below the tropopause will carry the average saturation mixing ratio of a subdomain that contains both stratospheric and tropospheric air. This average can be particularly unrepresentative of the actual (tropospheric) saturation mixing ratio that the parcel saw at last saturation. We have found that this can lead to large errors. Omitting the tracers associated with the top subdomains from the humidity reconstruction also induces an error, but it is a smaller one, in general, throughout the tropospheric levels below around 200 hPa. If we were interested in looking closely at the levels around the tropopause, we could do so by increasing the resolution of the tracers (decreasing the subdomain size) or, potentially, by incorporating a distinction between tropospheric and stratospheric air into the computation in some other way.

### 3. Idealized model

#### a. Model configuration

We first apply our diagnostic technique to an idealized model based on the dynamical core of the Flexible Modeling System (FMS) developed at the Geophysical Fluid Dynamics Laboratory. This model solves the hydrostatic primitive equations in sigma coordinates (20 equally spaced vertical levels) using the spectral transform method in the horizontal, Simmons and Burridge (1981) finite differencing in the vertical, and an Asselin-filtered semi-implicit leapfrog scheme for time integration. The results presented here were computed at a T42 spectral resolution. Similar results were obtained for a T85 model, indicating that the essential dynamics of the large-scale circulation are resolved at T42.

The model is forced by Newtonian relaxation of the temperature toward a prescribed, zonally symmetric, equilibrium temperature (Held and Suarez 1994) of the form:

$$T_{\text{eq}} = \max \left\{ T_{\text{st}}, \left[ (T_0 - (\Delta T)_y \sin^2(\phi)) - (\Delta \theta)_z \cos^2(\phi) \log \left( \frac{p}{p_0} \right) \right] \left( \frac{p}{p_0} \right)^\kappa \right\}, \quad (8)$$



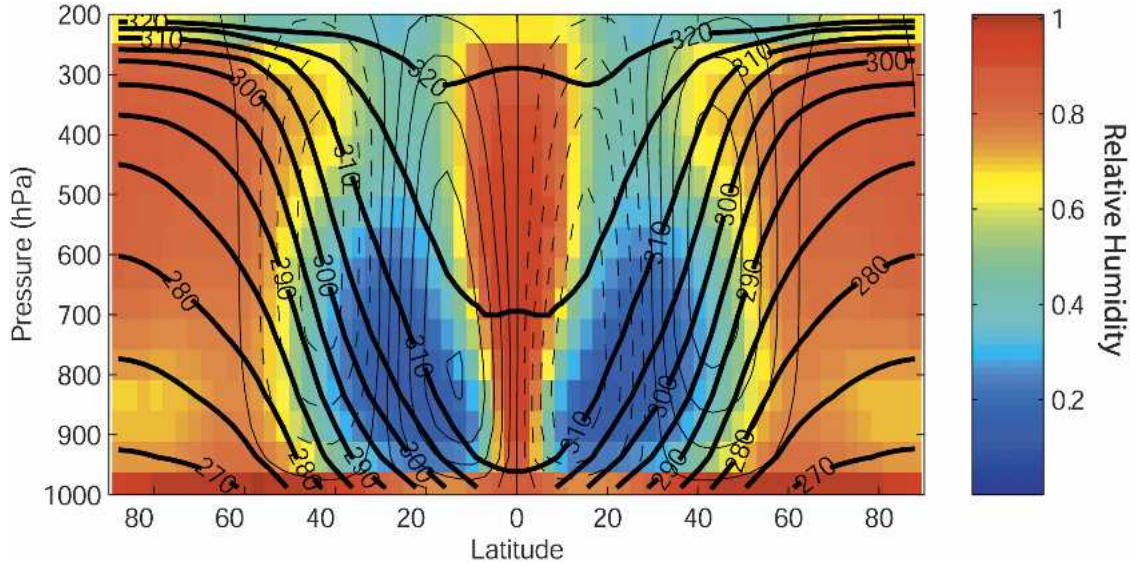


FIG. 2. Zonal-mean fields calculated from FMS with Held-Suarez forcing and large-scale moisture advection and condensation. Relative humidity shown in color; meridional streamfunction in thin contours (negative values are dashed); potential temperature (K) in thick contours.

where  $\phi$  is the latitude,  $T_{st}$  is the stratospheric temperature,  $T_0$  is the equilibrium temperature at the surface at the equator,  $(\Delta T)_y$  is the horizontal equator-to-pole temperature gradient, and  $(\Delta\theta)_z$  controls the static stability. The values used in this study are (in kelvin):  $T_{st} = 200$ ,  $T_0 = 315$ ,  $(\Delta T)_y = 60$ ,  $(\Delta\theta)_z = 10$ .

Planetary boundary layer drag is represented by Rayleigh damping. The frictional damping rate at the surface is  $1.0 \text{ day}^{-1}$  and decays linearly to the top of the nominal planetary boundary layer at  $\sigma = 0.7$ . All of the results here are 2800-day averages taken from a 3000-day run, with the first 200 days of integration discarded.

The tracer advection algorithm is a piecewise parabolic scheme in the vertical (Colella and Woodward 1984) and piecewise linear in the horizontal (van Leer 1979). Since the spectral model uses the log of the surface pressure as a prognostic variable, tracer mass cannot be conserved exactly. Instead, we use the advective form of the tracer equation in the faux flux form:

$$\mathbf{v} \cdot \nabla \xi = \nabla \cdot (v\xi) - \xi \nabla \cdot \mathbf{v}, \tag{9}$$

treating the first term on the rhs on the sphere following Lin and Rood (1996) and the second term in such a way that a uniform tracer remains exactly uniform.

The strongly discontinuous nature of the tracers (see Fig. 3) may pose a problem for some tracer advection schemes. As one basic check, we performed a simple experiment in which each tracer was set to 1 in its own subdomain and 0 elsewhere (discontinuous at the subdomain edges) at an initial time, and then advected for

one year with no imposed sources or sinks. In the case of perfect conservation, the global integral of the sum of all tracers should remain exactly 1. After a year, the global integral of the tracers in our model increased 1.5%. On time scales more relevant to water vapor (on the order of a month or so), the global integral varied by less than 0.5%. We thus conclude that the lack of strict conservation is not likely to be a significant source of error in our study. While this does not prove that numerical errors are necessarily small locally, it does indicate that any such errors do not have a strong impact on global conservation.

For the moist physics, we consider only the large-scale advection and condensation of a passive water vapor tracer. No latent heat is released upon condensation and there is no convective parameterization in the model. Water vapor is introduced as a fixed flux in the form  $E = E_0 \cos^2(\phi)$ , where  $E$  is the surface moisture flux and  $E_0$  is the maximum moisture flux. Here  $E_0 = 2.3 \times 10^{-5} \text{ kg m}^{-2} \text{ s}^{-1}$  which corresponds to a maximum moisture flux of about  $2.5 \text{ mm day}^{-1}$ . This flux is deposited in the lowest 50 hPa of the model.

At each time step, the relative humidity (RH) is calculated in each cell. If that cell is saturated, the excess moisture is removed and is assumed to rain out immediately; no condensate is carried in the model.

*b. Moisture fields*

We first describe some of the zonal-mean fields produced by this idealized moist GCM. In the RH field

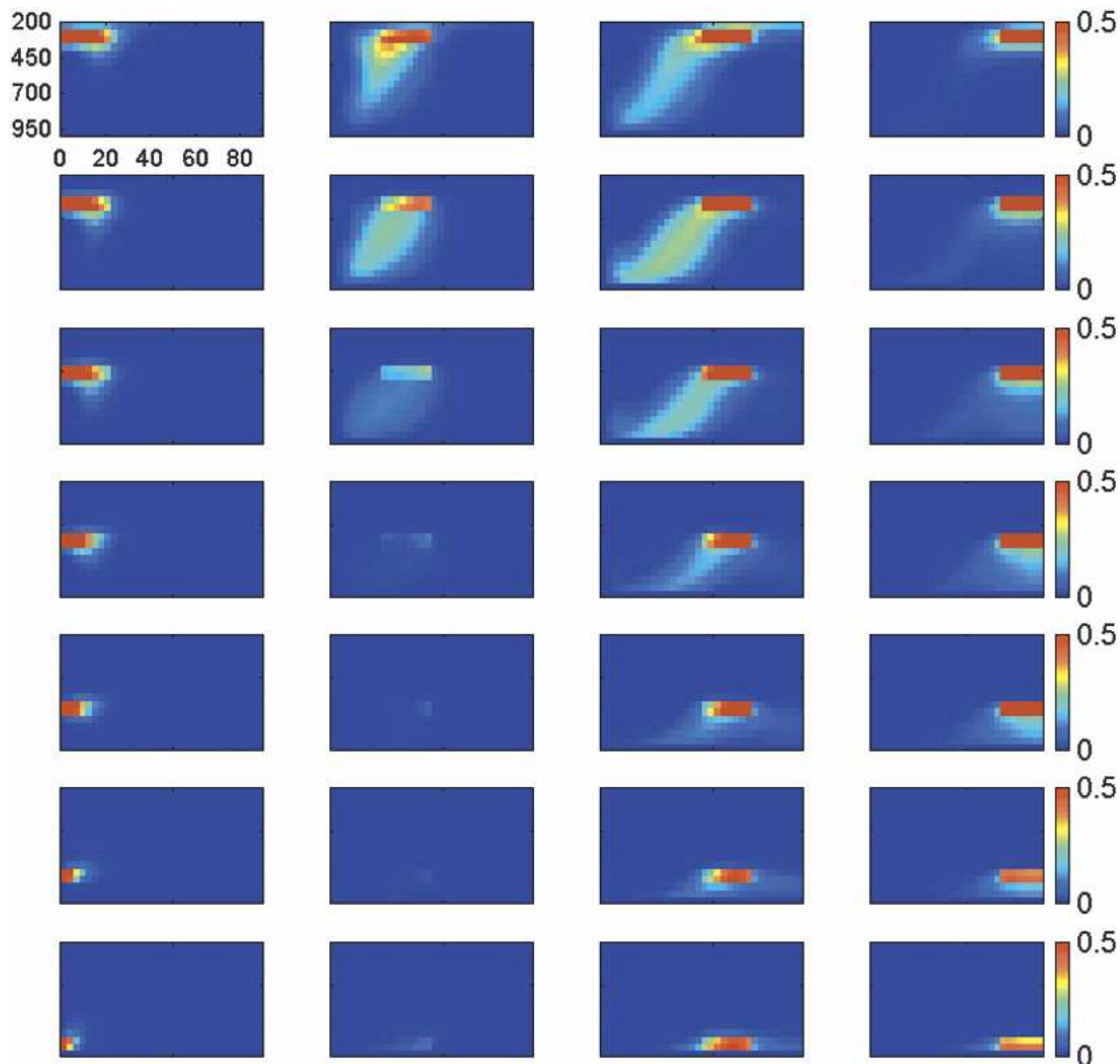


FIG. 3. The time mean and zonal mean of the 28 tracers used in this calculation. Horizontal axes are latitude ( $^{\circ}$ ); vertical axes are pressure (hPa). Colorbar indicates tracer concentration.

(Fig. 2), a very humid ( $RH > 90\%$ ) narrow equatorial zone is bounded by very dry air ( $RH < 20\%$ ) out to about  $40^{\circ}$  latitude. The relative humidity of the extratropics is variable, but generally around 80%.

The streamfunction (Fig. 2, thin contours) for the zonal-mean meridional circulation shows the expected form, including Hadley and Ferrell cells. As expected, the regions of very low RH correspond to regions of downward motion in the overturning circulation. Because no latent heat is released during condensation in our model, the potential temperature field (Fig. 2, thick contours) is that obtained from the standard Held–Suarez configuration.

While this simple model configuration should not be expected to reproduce the climatological details of the

real atmosphere, the overall humidity distribution is at least qualitatively realistic, with a moist equatorial zone bounded by a very dry subtropical region coincident with the downward limb of the meridional overturning circulation, though the extratropics are rather more humid than observed in the real atmosphere (Peixoto and Oort 1992).

### c. Tracer diagnostics

For the tracer diagnostics in the idealized model, each domain spans  $\pi/8$  radians of latitude and two vertical levels (about 100 hPa). Figure 3 shows the time mean and zonal mean of the 28 tracer fields obtained from the idealized GCM. These fields indicate the transport pathways that air parcels take between one

instance of saturation and the next. Some tracers have significant values outside of their associated subdomains, while others do not. In most of the tracer fields, the location of the associated subdomain is easily seen as a concentrated, well-defined zone of relatively high tracer concentration.

The equatorial tracers have large values within their own subdomains, but nearly vanish elsewhere. The tracer fields from the upper subtropical and midlatitude troposphere, in contrast, have prominent sloping plumes of nonzero tracer concentration that descend almost to the surface, while the tracers from the lower subtropical troposphere have very low values everywhere.

These results suggest a relatively straightforward physical interpretation in terms of interactions between the meridional overturning circulation and transport along isentropic surfaces (see Fig. 2). In general, air is saturated by adiabatic cooling during ascent in the overturning circulation. Because the air in the deep Tropics remains saturated throughout its ascent, the equatorial tracers are mostly confined to their respective subdomains; as soon as the air ascends into the next subdomain, it is saturated again, thus resetting the tracers associated with the other subdomains.

Air parcels that are last saturated in the upper levels then descend as they diabatically cool (by Newtonian cooling here, representing radiation) in the subtropical branch of the Hadley and Ferrell circulations, as indicated by the Eulerian-mean streamfunction in Fig. 2. As they do so, however, they are likely to get caught up in extratropical eddies, which sweep them upward and poleward and then back downward and equatorward, on approximately isentropic trajectories. These excursions largely cancel in the Eulerian mean, but are important for drying the air because temperatures, and thus saturation vapor pressures, are quite low at the poleward extremes reached by the air parcels. Much water vapor is therefore wrung out of parcels during their poleward transport (Yang and Pierrehumbert 1994). An overlay of the tracer fields with a plot of potential temperature (not shown) shows that the descending plumes of upper-level subtropical tracers lie almost exactly along isentropic surfaces. This indicates that, in this idealized model, the diabatic descent of dry air directly from the top of the tropical ascent region contributes relatively weakly to the production of dry air, compared to isentropic transport by midlatitude eddies. The plume structures indicate that much of the air in the subtropics was last saturated in the middle and upper troposphere of the higher subtropical or lower extratropical latitudes, roughly in the subtropical jet regions.

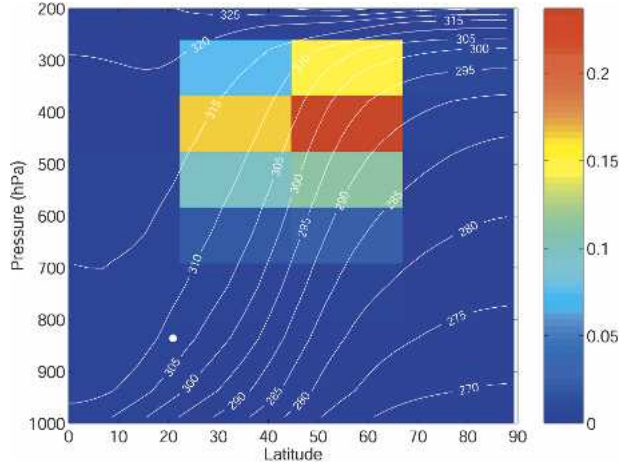


FIG. 4. The probability distribution function for location of last saturation for reference point (marked by white dot). The reference point is the driest part of the subtropics, with relative humidity at about 11%. Contours are potential temperature in degrees kelvin.

The probability distribution for a reference location in the dry subtropical zone (Fig. 4) further illustrates this point. In this plot, the color in each subdomain represents the value of that subdomain’s tracer at the reference location. The plot shows that the location of last saturation for the reference location (at 835 hPa, marked by the white dot) was primarily in higher, poleward subdomains, consistent with descent along isentropic surfaces. Vertical, cross-isentropic transport does make some contribution, but a relatively small one.

The tracers can be used to produce diagnostics that summarize some aspects of the dynamical picture just described. Figure 5a shows the average temperature of last saturation ( $T_s$ ). This is computed by multiplying the tracers with the temperature field rather than the saturation mixing ratio, that is, computing the rhs of (7) with temperature replacing the mixing ratio, omitting the source term, and normalizing by the sum of the contributing tracers:

$$T_s(\phi, p) = \frac{\sum_i \hat{T}_i(\phi, p)T_i(\phi, p) + \sum_i \check{T}_i(\phi, p)\langle T_i \rangle}{\sum_i T_i} \quad (10)$$

Note the band of low  $T_s$  in the Tropics and subtropics (adjacent to the equatorial zone of high  $T_s$ ) that descends to 900 mb. These temperatures correspond to the temperature near the top of the troposphere.

Figure 5b shows the warming experienced since last saturation ( $T - T_s$ ). The driest regions of the Tropics and subtropics have warmed by 40° or more since last saturation; this warming, coupled with the cold saturation temperature, is responsible for the extremely low

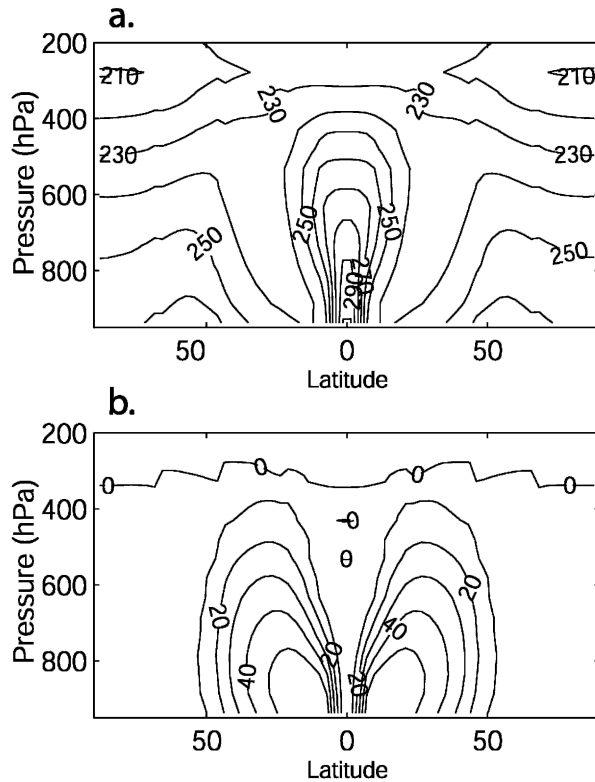


FIG. 5. (a) Contour plot of  $T_s$ , the temperature of last saturation; (b)  $(T - T_s)$ , the amount of warming since last saturation. Contours are potential temperature in degrees kelvin.

relative humidities in these regions. These two diagnostics,  $T_s$  and  $T - T_s$ , convey information about how specific and relative humidities, respectively, are set. Figure 5b looks qualitatively very similar to, but differs quantitatively from, a plot of the dewpoint depression,  $T - T_d$ , (not shown) with  $T_d$  the dewpoint. Since the temperature equals the dewpoint at last saturation,  $T - T_s$  would be identical to  $T - T_d$  except for two effects. The first is that the pressure has changed since last saturation (which changes the vapor pressure, and thus the dewpoint, even though mixing ratio is conserved). The second is that not all air has been saturated since last contact with the surface. Particularly at low levels, the source term, representing air that has not been saturated since last contact with the surface, tends to moisten the air and thus raise  $T_d$ , while having no effect on  $T_s$ . Because of these two effects, of which the second is quantitatively more important,  $T - T_d$  is generally smaller than  $T - T_s$ , by over 20 K in the driest regions, but the two fields have nearly identical spatial structure.

#### d. Reconstruction of relative humidity using tracers

The reliability of the diagnostics described above depends on the assumption that the tracer fields accu-

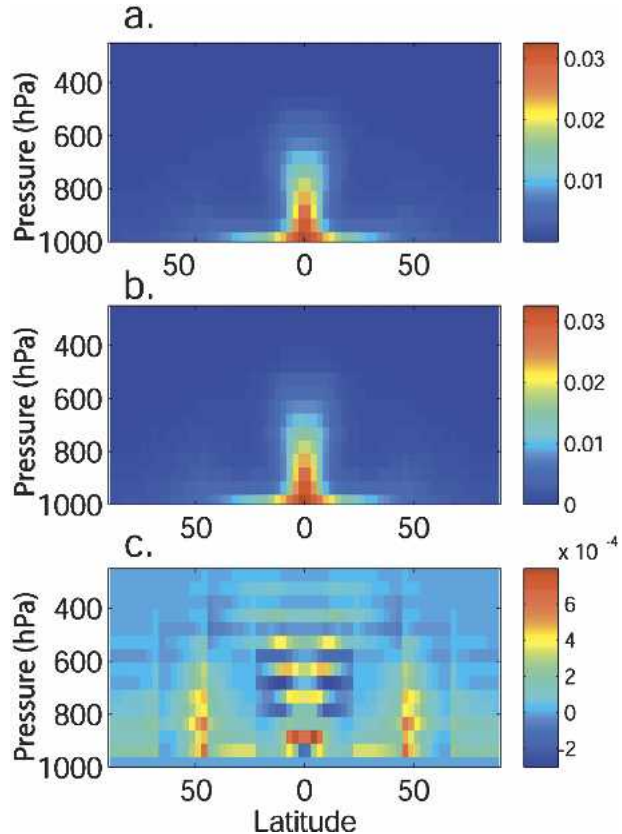


FIG. 6. (a) Mixing ratio calculated from the full model ( $\text{kg kg}^{-1}$ ); (b) mixing ratio reconstructed from tracers; (c) difference between reconstructed mixing ratio and model mixing ratio.

rately reflect the underlying humidity field. To test this, we now use the tracer fields to reconstruct the relative humidity fields using Eq. (7).

Figure 6a shows the mixing ratio field calculated in the full model, the reconstructed mixing ratio is shown in Fig. 6b, and the difference between the reconstruction and the model in Fig. 6c. The largest absolute differences in mixing ratio are at the lowest levels of the deep Tropics, largely because the mixing ratio itself is largest there. Figure 7a shows the RH fields calculated in the full model, Fig. 7b shows the RH reconstructed from the tracers, and the difference between the reconstruction and model in Fig. 7c. The reconstructed RH fields are generally close to, although slight overestimates of, the original simulated RH. The reconstruction in the driest region of the subtropics is quite good however: the model RH here is 11.2% while the reconstructed RH at the same point is 11.6% (reference location indicated in Fig. 7a).

Some of the errors are due to the averaging processes involved in the reconstruction process. The humidity is critically dependent on the minimum temperatures en-



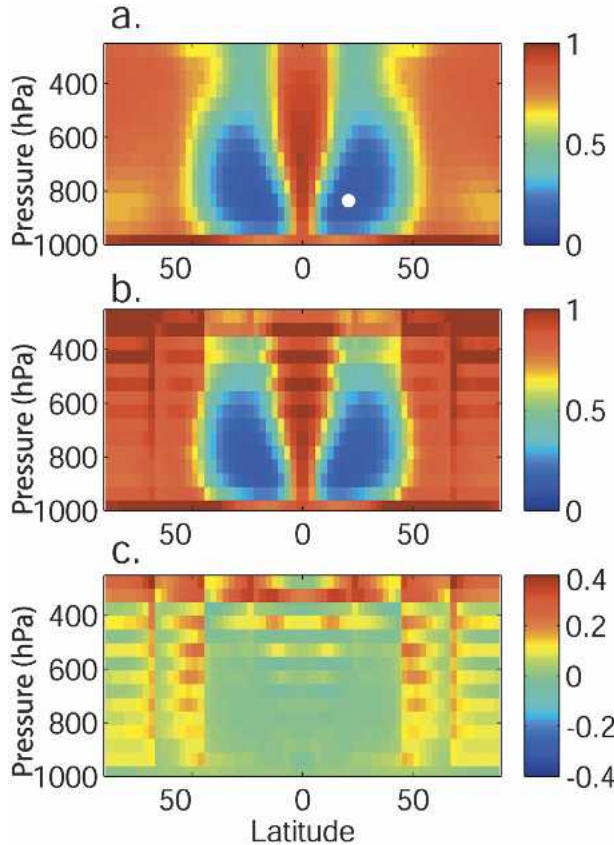


FIG. 7. (a) Relative humidity calculated from the full model; the white dot indicates the reference point mentioned in text; (b) RH reconstructed from tracers; (c) difference between reconstructed and model RH.

countered by air parcels, and averaged mixing ratios of last saturation,  $\langle r_i^* \rangle$ , will always be at least somewhat unrepresentative of the actual minima encountered by individual parcels. As mentioned earlier, the resulting errors do not generally vanish in the reconstruction of the zonal and time mean mixing ratio. There is also an obvious granularity in the reconstructed humidity fields, in which the subdomains used to define the tracers are apparent. This results primarily from the different treatment of the local and nonlocal tracers. Figure 8 shows the tracer fields, broken into local (Fig. 8a), nonlocal (Fig. 8b), and the sum of all tracers (Fig. 8c). The sum of all tracers is close to 1 over most of the domain, as expected, with reduced values near the surface due to the source term, and at upper levels in the subtropics due to our omission of tracers in the uppermost troposphere and stratosphere. There is also a very weak granularity, which we believe to be due to numerical advection errors associated with the very strong and nonlinear tracer gradients at the subdomain edges (see Fig. 3). The sums of the local and nonlocal tracers

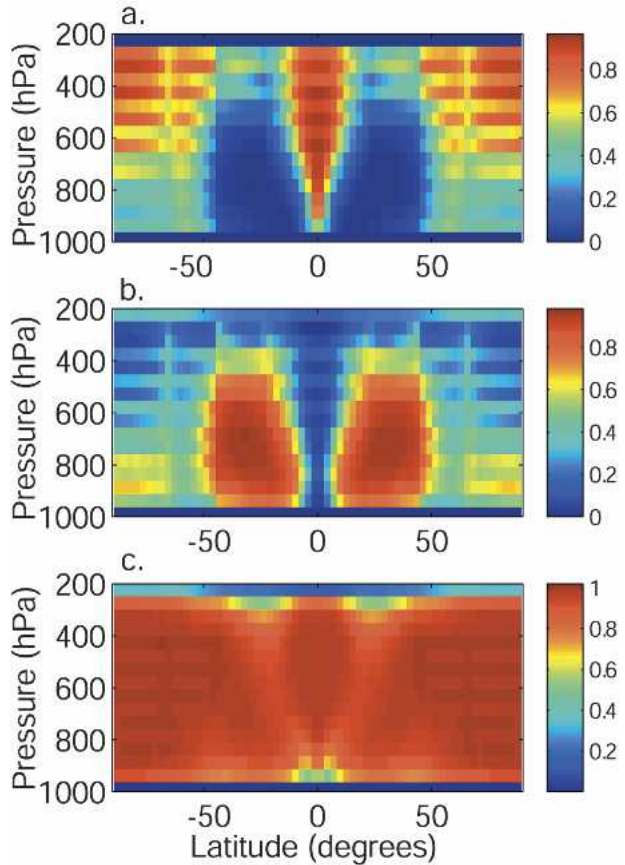


FIG. 8. Relationship of (a) local, (b) nonlocal, and (c) sum of all tracer components.

(Figs. 8a,b), on the other hand, have much stronger granularities. We do not understand these granular structures in great detail, but simply observe that they largely cancel when the local and nonlocal tracers are added together, yielding the much more nearly smooth structure in Fig. 8c. When the tracer fields are used to reconstruct the water vapor field, however, the different treatments of the local and nonlocal tracers lead to the persistence of the granularity in the reconstruction, as the local tracers are multiplied by the local  $r^*$ , which is smooth, while the nonlocal tracers are multiplied by the averages  $\langle r^* \rangle$ , which change discontinuously from one subdomain to the next. Using the latter for both tracers might be more consistent, but yields a result that is less accurate overall. If we could afford to reduce the subdomain size to the model grid size, we expect the granularity in all fields would vanish.

While the errors in the reconstructed humidity fields are not negligible, the overall reconstruction is largely representative of the original model humidity fields. The humidity in the dry subtropical zones is especially well reproduced by the reconstruction and, given that

our main interest is in understanding the controls on the humidity in these dry regions, we conclude that this tracer technique works well enough to warrant its application to more realistic datasets.

#### 4. Application to reanalysis data

##### a. Model configuration

We now apply the tracer technique to the NCEP–NCAR reanalysis data (Kalnay et al. 1996) using an offline tracer transport model, the Model of Atmospheric Transport and Chemistry, (MATCH; Rasch et al. 1997), which advects tracers with archived wind and temperature fields and includes algorithms for large-scale tracer transport. MATCH also has its own hydrologic cycle and has parameterizations for cloud physics, convection, and planetary boundary layer processes.

MATCH performs a linear interpolation between the times of the available input data (available at 6-h intervals for the NCEP–NCAR reanalysis data used here) and the current time step. For the results presented here, we used a 30-min time step. The input data determines MATCH's spatial resolution and grid discretization. All of the results presented here use the standard NCEP–NCAR reanalysis resolution of 192 longitude points and 94 latitude points on a Gaussian grid with 28 unevenly spaced hybrid sigma vertical levels.

MATCH's tracer advection scheme is based on the semi-Lagrangian transport (SLT) algorithm described by Rasch and Williamson (1990). Because SLT schemes are inherently nonconservative, MATCH employs the mass fixer of Rasch et al. (1995) to explicitly enforce mass conservation. MATCH also uses a vertical eddy diffusion parameterization to represent subgrid-scale turbulent mixing and a nonlocal planetary boundary layer scheme. The cloud physics parameterization in MATCH is based on the parameterization developed for version 3 of the NCAR Community Climate Model (CCM3) by Rasch and Kristjansson (1998) and predicts the mass of condensate for liquid and ice phases. The conversion from condensate to precipitation is computed using a bulk microphysical model.

The convective parameterization in MATCH is based on that in the NCAR CCM3 (Hack et al. 1998), which uses the deep cumulus scheme of Zhang and McFarlane (1995) followed by application of the Hack (1994) local convective transport scheme. The Zhang–McFarlane scheme employs updraft and downdraft plume models that entrain and detrain laterally. Tracers are advected by the compensating mass flux produced by the convection schemes as well as by the large-scale flow. By default, MATCH's convective parameterization does not remove tracers during convec-

tion, but MATCH does include an adjustable parameter to allow a fixed fraction of tracer to be removed during convection.

For the results presented here, we use a tracer configuration consisting of 100 zonally symmetric tracer domains between latitudes 50°N and 50°S. The limited meridional extent is necessary to limit the overall computational expense. Each domain spans 10° of latitude and two vertical levels. The source tracer in this calculation is set to the value of the water vapor mixing ratio in the lowest reanalysis level, which spans 30 hPa. We use MATCH's internal water vapor field, rather than that of the reanalysis itself, to determine when saturation has occurred in our tracer calculations. To account for the possibility of subgrid-scale saturation, we assume that saturation has occurred when the MATCH relative humidity exceeds 90%. The results discussed below are not sensitive to the precise value of this threshold.

We ran MATCH with our diagnostic tracers for reanalysis dates from 1 November 2001 through 1 March 2002. The tracers require a spinup of about three to four weeks, so we discarded the first month of the calculation to produce a time mean for December–February (DJF) 2001/02. MATCH's hydrologic cycle yields a total column water vapor that generally matches, though slightly underestimates, that derived from the Tropical Rainfall Measuring Mission (TRMM) Microwave Imager (TMI) satellite data from the same time period (not shown; Wentz 1997).

##### b. Reanalysis results

First, we show how the tracers can be used to reconstruct the zonal-mean relative humidity (Fig. 9). The reconstruction of the relative humidity in the planetary boundary layer and subtropical dry zones is generally accurate. The MATCH RH at the driest part of the dry zone (reference point indicated by the white circle in Fig. 9a, located at 20°N latitude and 632 hPa) is 22%, with a mixing ratio of  $1.6 \times 10^{-3}$ , while the reconstructed RH at the same point is 24%, with a mixing ratio of  $1.7 \times 10^{-3}$ . Slightly higher in the dry zone (reference point indicated by the white square in Fig. 9a, located at 20°N latitude and 500 hPa), the zonal-mean RH is 26%, with a mixing ratio of  $1.0 \times 10^{-3}$ , while the reconstructed RH is also 26%, with a mixing ratio of  $1.0 \times 10^{-3}$ .

In contrast, the reconstructed relative humidity in the upper troposphere is generally much higher than that calculated by MATCH. Most of this error is due to excessive convective transport of tracer from the PBL into the upper troposphere. As described above, MATCH's convective parameterization does not, by

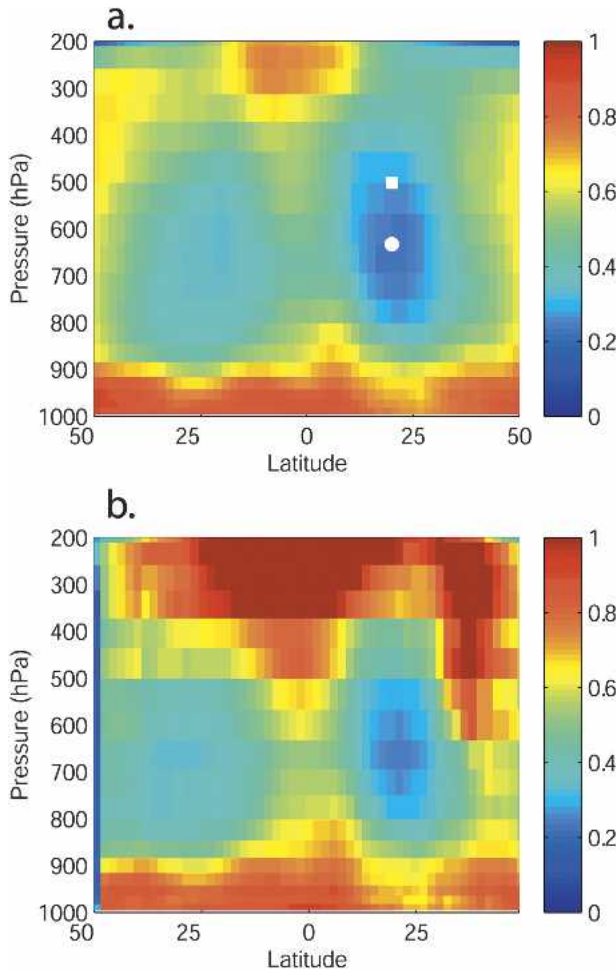


FIG. 9. DJF 2001/02 zonal-mean RH: (a) MATCH hydrologic cycle applied to NCEP-NCAR reanalysis data; (b) reconstructed from tracer calculation.

default, remove tracers during convection. Our tracers are meant to represent water vapor, however, and so should largely rain out during ascent in parameterized updrafts. The default parameterization, used in the calculation whose results are shown in Fig. 9, thus transports too much tracer into the upper levels, resulting in the excess in the tropical upper troposphere. An adjustable parameter in the scheme allows a fixed fraction of the tracer to be removed by convection. An additional experiment (not shown), in which this parameter is set to zero, so that all of the tracer rains out during convection, overcompensates for this error, yielding a reconstructed humidity that is too dry in the upper troposphere. The reconstructed RH in the dry zone is not significantly affected by the details of convective tracer transport, however, suggesting that the humidity of the dry regions of the subtropical free troposphere can be understood, to first order, by considering only the

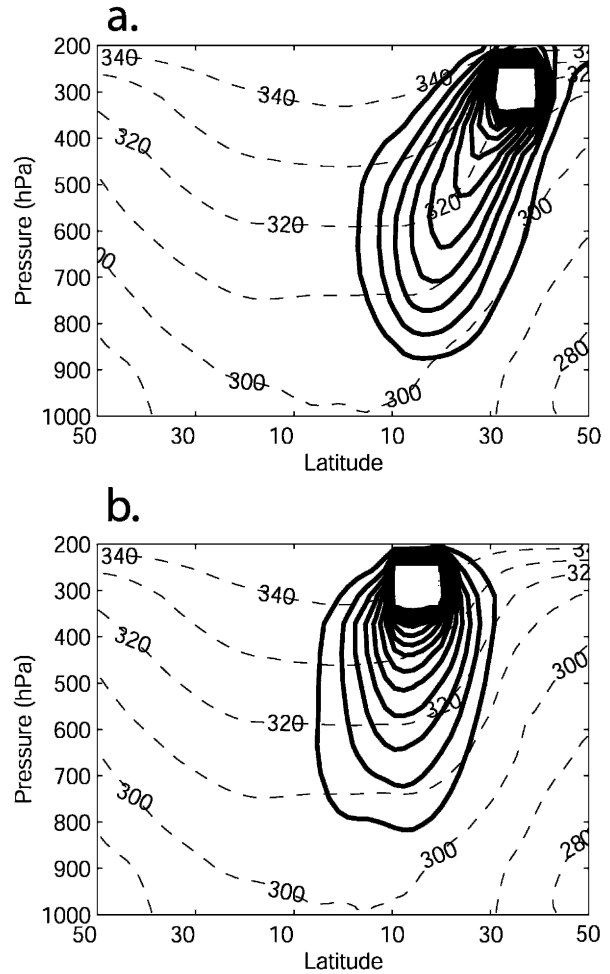


FIG. 10. Zonal-mean tracers from NCEP-NCAR reanalysis data for DJF 2001/02, computed with MATCH offline tracer transport model. Solid contours are tracer concentration; the outermost contour in each plot is 0.02. Dashed lines are potential temperature; contour interval is 10 K. (a) Extratropical subdomain, defined between 30° and 40°N and 258 and 312 hPa; (b) tropical subdomain, defined between 10° and 20°N and 258 and 312 hPa.

large-scale advection and condensation of water vapor, consistent with previous studies (Sherwood 1996; Salathé and Hartmann 1997; Pierrehumbert and Roca 1998; Dessler and Sherwood 2000).

It is instructive to focus initially on the zonal-mean tracers associated with two subdomains in the Northern Hemisphere, one in the extratropics and the other in the Tropics. The extratropical subdomain (Fig. 10a) spans a region between 30° and 40°N latitude and 258 and 312 hPa vertically. A zone of high tracer concentration projects downward and equatorward from the extratropical subdomain, centered along the 320-K isentrope. Tracer concentrations in excess of 0.05 extend as far away as 700 hPa and 10°N. The tropical



subdomain (Fig. 10b) spans a region between 10° and 20°N latitude and 258 and 312 hPa vertically. In comparison with the extratropical region, the nonlocal tracer concentration emanating from the tropical region is slightly weaker, with the zone of highest tracer concentration projecting directly downward, across isentropes.

In contrast to the tracers in the idealized model, whose statistics are zonally symmetric due to the zonal symmetry of the Held–Suarez boundary conditions and forcings, the tracers derived from the reanalysis data exhibit zonal variability even in the time mean. Focusing on the influence of the extratropical and tropical subdomains (defined above) on the humidity at 632 hPa (Fig. 11a), we see that they contribute to the humidity at 631 hPa in different regions. Contributions from the extratropical isentropic path (Fig. 11b) are well correlated with regions of low relative humidity in the western tropical Atlantic and the eastern Pacific. In contrast, the tropical subdomain (Fig. 11c) contributes less unsaturated air to this level overall than does the extratropical subdomain. An exception is the dry region over the Horn of Africa, where the tropical domain contributes almost 15% of the unsaturated air. While these zonal asymmetries are significant, the figure also clearly shows that there is a substantial zonally symmetric component to the tracer distributions, so analyzing zonal-mean features of the tracer fields is justified.

Zonal-mean probability distribution functions show the contributions of air last saturated in different regions to the humidity at selected reference points. Figure 12 shows the zonal-mean probability distribution function (PDF) for a reference point near the top of the subtropical dry zone (Fig. 12a; the location of the point is given by the white square in Fig. 9), and lower down, in the driest part of the subtropical dry zone (Fig. 12b; the location of the point is given by the white circle in Fig. 9). About 53% of the air at the top of the dry zone (Fig. 12a) was last saturated north of 20°N and above 516 hPa, while about 60% of the air in the driest part of the subtropics (Fig. 12b) was last saturated north of 20°N and above 516 hPa. The air from the high extratropical zones has descended to the reference points along approximately isentropic paths. The upper part of the dry zone also receives a substantial fraction of its unsaturated air via diabatic descent, while the central part of the dry zone receives less air via this cross-isentropic path.

While the PDFs show which regions contribute most of the unsaturated air to the reference points, they do not by themselves provide any information about the relative dryness of that air. Figure 13 shows a scatterplot of the probability of last saturation for each sub-

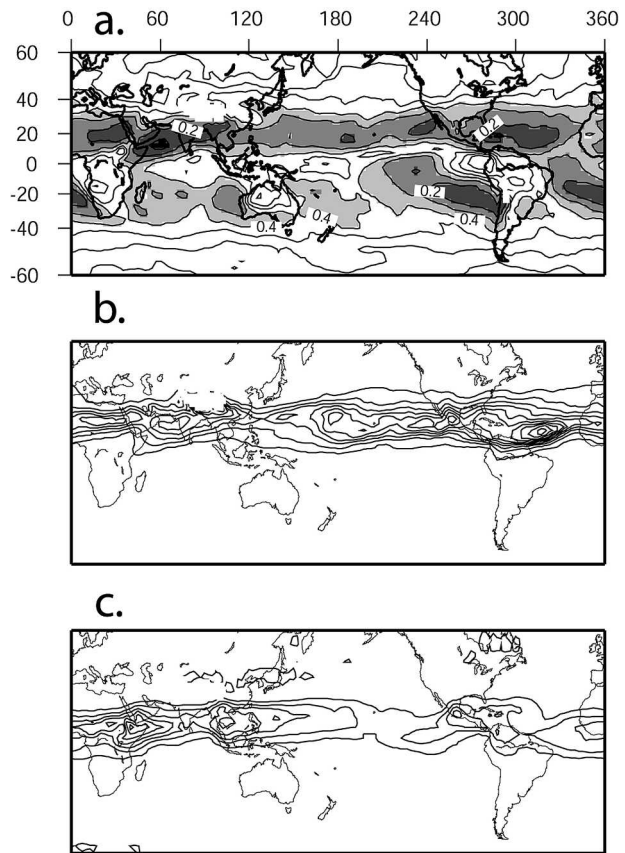


FIG. 11. (a) DJF 2001/02 RH at 633 hPa, derived from MATCH and NCEP–NCAR reanalysis data. Contour interval is 0.1; RH below 40% highlighted with gray shading. (b) Tracer concentration on the 633-hPa surface from extratropical subdomain defined in Fig. 10. Contour interval is 0.02. (c) As in (b) except for the tropical subdomain defined in Fig. 10. Regions where topography intersects the 633-hPa surface are masked.

domain in the Northern Hemisphere against the zonal-mean water vapor mixing ratio for that subdomain. These quantities are computed for the reference point in the driest part of the subtropics (marked by the white circle in Fig. 9). This figure thus illustrates the zonal-mean probability of water vapor mixing ratio at last saturation for the reference point. The domains north of 20°N are the sites of the highest probability of last saturation for the reference location and generally contribute extremely dry air to the dry zone, with water vapor mixing ratios up to an order of magnitude less than the mixing ratio at the reference point. The weighted mean mixing ratio from the contributing regions north of 20°N and above 516 hPa is about  $6.2 \times 10^{-4}$ . Most of this air descends to the dry zone along isentropic paths. In contrast, the air south of 20°N, which includes air that descends via diabatic cooling as well as air that ascends into the dry zone, is up to an



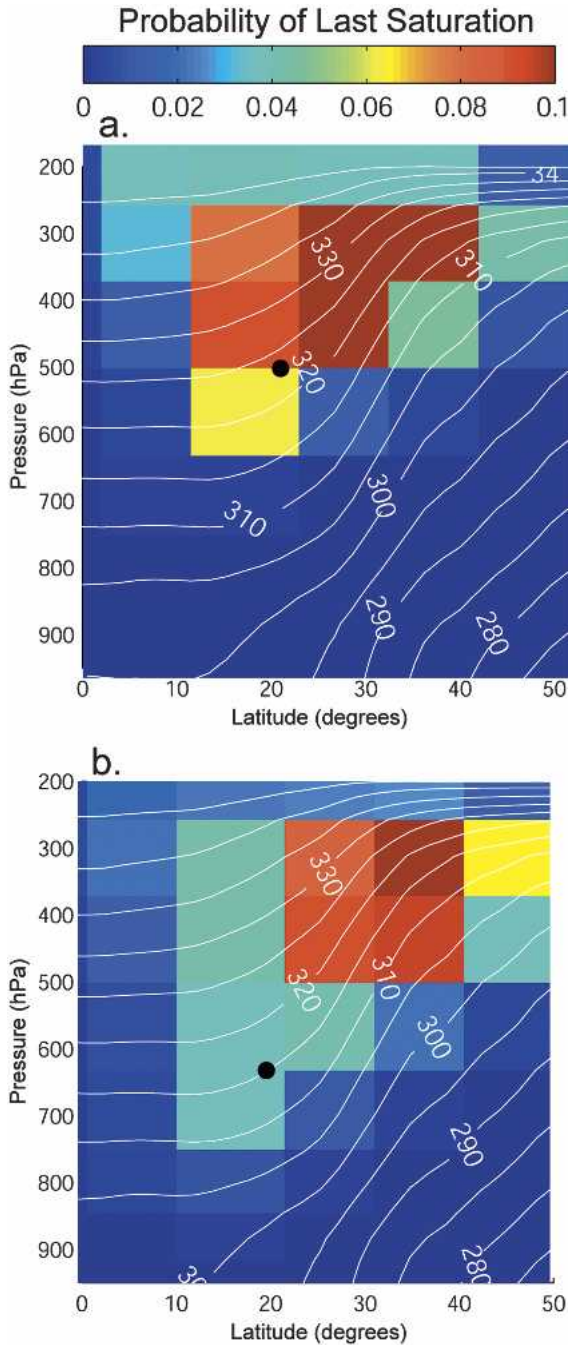


FIG. 12. Zonal-mean probability of location of last saturation for two reference points: (a) upper region of dry zone (location of point shown by white square in Fig. 9a); (b) central region of dry zone (location of point shown by white circle in Fig. 9a). Contours are potential temperature in degrees kelvin.

order of magnitude more moist than the air at the reference point with a weighted-mean mixing ratio of about  $3.5 \times 10^{-3}$ . All of the air last saturated below 516 hPa (shown by open symbols) is substantially more moist than the air at the reference point. Tropical lower

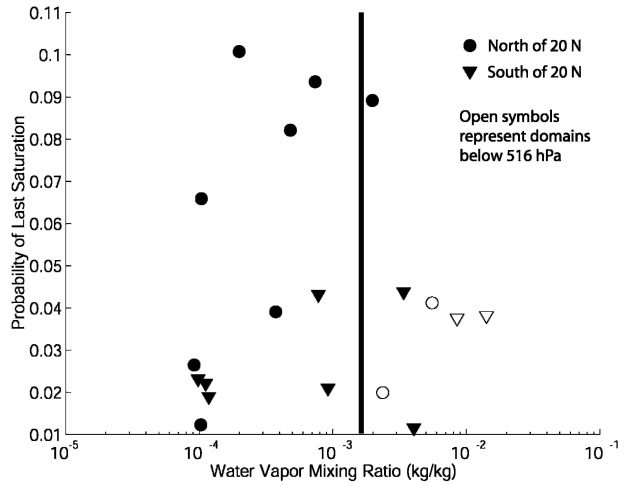


FIG. 13. Zonal-mean probability of water vapor mixing ratio at last saturation for reference site in the dry zone of the subtropics (location of reference point shown by white circle in Fig. 9a). Contributing subdomains north of 20°N are indicated by circles and contributing subdomains south of 20°N are indicated by triangles. Open symbols indicate domains below 516 hPa. Vertical bar indicates water vapor mixing ratio at the reference point.

tropospheric air has the highest mixing ratio of any contributing region, with a mixing ratio of  $1.4 \times 10^{-2}$ .

### 5. Discussion and conclusions

The general picture that emerges from the above results is that the dryness of the subtropics is primarily controlled by midlatitude eddies that isentropically dehydrate subtropical air, which is subsequently mixed with moister tropical air. Direct diabatic descent of air from the outflow of the Hadley circulation appears to play a secondary role in setting the dryness of the subtropics. As air descends diabatically in the subtropics, it is likely to get caught up in midlatitude eddies that bring it upward and poleward along isentropes, saturate it at low temperature, thereby dehydrating it, and then return it to the subtropics, in a way that is invisible from the point of view of the Eulerian-mean flow, or even (to the extent that the eddies are transient) the time-mean trajectories used by Salathe and Hartmann (1997). Since isentropic motions tend to be rapid compared to cross-isentropic motion, the time scale of this isentropic, extratropical dehydration is apparently short compared to that which would occur due to the mean diabatic descent alone, and thus the former is the dominant process.

This extratropical dehydration must be considered in arguments about how subtropical water vapor will respond to global climate change. Subtropical humidity

could change independently of any tropical mechanism if changes in extratropical eddies change the statistics of the extratropical drying. Similarly, some tropical mechanisms that have been debated, such as changes in the height at which air detrains from deep tropical convection (Held and Soden 2000), may be less important than previously thought if parcels last saturated in convective towers are destined to be quickly saturated again in midlatitude eddies at colder temperatures.

To summarize, we have presented a technique for diagnosing the mechanisms that control water vapor in GCMs and reanalysis data. In this technique, the atmosphere is divided into subdomains, and tracers associated with each subdomain track the air that was last saturated there. From the spatial distributions of these tracers and the temperature field, we can construct a number of useful diagnostics regarding the location and mixing ratio of last saturation.

The technique was first applied to an idealized model that considered only large-scale advection and condensation of water vapor. The resulting tracers were successfully used to reconstruct the relative humidity and illustrate the spatial distribution of last saturation within the model.

The technique was then applied to NCEP–NCAR reanalysis data for DJF 2001/02. The lowest zonal-mean relative humidity for this period was 22%, with a mixing ratio of  $1.6 \times 10^{-3}$ , and was located at 20°N latitude and 632 hPa. Approximately 60% of the air at this location was last saturated north of 20°N and above 516 hPa, most of which descended into the subtropics along isentropic paths. The weighted-mean mixing ratio of this contributing air was  $6.2 \times 10^{-4}$ . In contrast, the contributing air south of 20°N had a weighted mean mixing ratio of  $3.5 \times 10^{-3}$  with the tropical lower troposphere contributing air with mixing ratios as high as  $1.4 \times 10^{-2}$ .

The main result of the reanalysis component of this study is that the dryness of the subtropical free troposphere (at least for the period under consideration) is largely controlled by extratropical eddies that dehydrate the air by transporting it isentropically to higher latitudes and altitudes and then back into the subtropics, where it is moistened by mixing with tropical air.

Future studies with this diagnostic will focus on understanding the seasonal and interannual variability of the controls on subtropical humidity and the possible changes in last saturation that may occur during global warming.

*Acknowledgments.* This research was supported by the David and Lucile Packard Foundation and by the Cooperative Institute for Climate Applications and Re-

search (CICAR) Award NA03OAR4320179 from the National Oceanic and Atmospheric Administration and the U.S. Department of Commerce. We thank Tapio Schneider for useful discussions and Phil Rasch and Natalie Mahowald for assistance with MATCH.

#### REFERENCES

- Colella, P., and P. Woodward, 1984: The piecewise parabolic method (PPM) for gas dynamical simulations. *J. Comput. Phys.*, **54**, 174–201.
- Dessler, A., and S. Sherwood, 2000: Simulations of tropical upper tropospheric humidity. *J. Geophys. Res.*, **105** (D15), 20 155–20 163.
- Ebert, E., U. Schumann, and R. Stull, 1989: Nonlocal turbulent mixing in the convective boundary layer evaluated from large eddy simulation. *J. Atmos. Sci.*, **46**, 2178–2207.
- Hack, J., 1994: Parameterization of moist convection in the NCAR Community Climate Model, CCM2. *J. Geophys. Res.*, **99**, 5551–5568.
- , J. Kiehl, and J. Hurrell, 1998: The hydrologic and thermodynamic characteristics of the NCAR CCM3. *J. Climate*, **11**, 1179–1206.
- Haine, T., and T. Hall, 2002: A generalized transport theory: Water-mass composition and age. *J. Phys. Oceanogr.*, **32**, 1932–1946.
- Hall, T., and R. Plumb, 1994: Age as a diagnostic of stratospheric transport. *J. Geophys. Res.*, **99**, 3539–3558.
- Held, I., and M. Suarez, 1994: A proposal for the intercomparison of the dynamical cores of atmospheric general circulation models. *Bull. Amer. Meteor. Soc.*, **75**, 1825–1830.
- , and B. J. Soden, 2000: Water vapor feedback and global warming. *Annu. Rev. Energy Environ.*, **25**, 441–475.
- Holzer, M., and T. Hall, 2000: Transit-time and tracer-age distributions in geophysical flows. *J. Atmos. Sci.*, **57**, 3539–3558.
- Kalnay, E., and Coauthors, 1996: The NCEP/NCAR 40-Year Reanalysis Project. *Bull. Amer. Meteor. Soc.*, **77**, 437–471.
- Kelly, K., A. Tuck, and T. Davies, 1991: Wintertime asymmetry of upper tropospheric water between the Northern and Southern Hemispheres. *Nature*, **353**, 244–247.
- Larson, V., 1999: The relationship between the transilient matrix and the Green's function for the advection–diffusion equation. *J. Atmos. Sci.*, **56**, 2447–2453.
- Lin, S.-J., and R. Rood, 1996: Multidimensional flux form semi-Lagrangian transport schemes. *Mon. Wea. Rev.*, **124**, 2046–2070.
- Peixoto, J., and A. Oort, 1992: *Physics of Climate*. AIP Press, 564 pp.
- Pierrehumbert, R., 1995: Thermostats, radiator fins, and the local runaway greenhouse. *J. Atmos. Sci.*, **52**, 1784–1806.
- , 1998: Lateral mixing as a source of subtropical water vapor. *Geophys. Res. Lett.*, **25**, 151–154.
- , and R. Roca, 1998: Evidence for control of Atlantic subtropical humidity by large scale advection. *Geophys. Res. Lett.*, **25**, 4537–4540.
- Rasch, P., and D. Williamson, 1990: Computational aspects of moisture transport in global models of the atmosphere. *Quart. J. Roy. Meteor. Soc.*, **116**, 1071–1090.
- , and J. Kristjansson, 1998: A comparison of the CCM3 model climate using diagnosed and predicted condensate parameterizations. *J. Climate*, **11**, 1587–1614.

- , B. Boville, and G. Brasseur, 1995: A three-dimensional general circulation model with coupled chemistry for the middle atmosphere. *J. Geophys. Res.*, **100**, 9041–9072.
- , N. Mahowald, and B. Eaton, 1997: Representations of transport, convection, and the hydrologic cycle in chemical transport models: Implications for the modeling of short-lived and soluble species. *J. Geophys. Res.*, **102** (D23), 28 127–28 138.
- Salathe, E. P., and D. L. Hartmann, 1997: A trajectory analysis of tropical upper-tropospheric moisture and convection. *J. Climate*, **10**, 2533–2547.
- Sherwood, S., 1996: Maintenance of the free-tropospheric tropical water vapor distribution. Part II: Simulation by large-scale advection. *J. Climate*, **9**, 2919–2934.
- Simmons, A., and D. Burridge, 1981: An energy and angular-momentum conserving vertical finite-difference scheme and hybrid vertical coordinates. *Mon. Wea. Rev.*, **109**, 758–766.
- Sobel, A., 1999: Diffusion versus nonlocal models of stratospheric mixing, in theory and practice. *J. Atmos. Sci.*, **56**, 2571–2584.
- Soden, B., 1998: Tracking upper tropospheric water vapor radiances: A satellite perspective. *J. Geophys. Res.*, **103** (D14), 17 069–17 081.
- Spencer, R., and W. Braswell, 1997: How dry is the tropical free troposphere? Implications for global warming theory. *Bull. Amer. Meteor. Soc.*, **78**, 1097–1106.
- Stull, R., 1984: Transient turbulence theory. Part I: The concept of eddy-mixing across finite distances. *J. Atmos. Sci.*, **41**, 3351–3367.
- , 1993: Review of non-local mixing in turbulent atmospheres: Transient turbulence theory. *Bound.-Layer Meteor.*, **62**, 21–96.
- Sun, D.-Z., and R. Lindzen, 1993: Distribution of tropical tropospheric water vapor. *J. Atmos. Sci.*, **50**, 1643–1660.
- van Leer, B., 1979: Toward the ultimate conservative difference schemes. V: A second order sequel to Godunov method. *J. Comput. Phys.*, **32**, 101–136.
- Wentz, F., 1997: A well-calibrated ocean algorithm for special sensor microwave/imager. *J. Geophys. Res.*, **102** (C4), 8703–8718.
- Yang, H., and R. Pierrehumbert, 1994: Production of dry air by isentropic mixing. *J. Atmos. Sci.*, **51**, 3437–3454.
- Zhang, G., and N. McFarlane, 1995: Sensitivity of climate simulations to the parameterization of cumulus convection in the Canadian Climate Centre general circulation model. *Atmos.–Ocean*, **33**, 407–446.